Optics Letters

Bit-efficient, sub-millisecond wavefront measurement using a lock-in camera for time-reversal based optical focusing inside scattering media

Yan Liu, Cheng Ma, Yuecheng Shen, and Lihong V. Wang*

Optical Imaging Laboratory, Department of Biomedical Engineering, Washington University in St. Louis, One Brookings Drive, St. Louis, Missouri 63130, USA
Corresponding author: lhwang@wustl.edu

Time-reversed ultrasonically encoded optical focusing measures the wavefront of ultrasonically tagged light, and then phase conjugates the tagged light back to the ultrasonic focus, thus focusing light deep inside the scattering media. In previous works, the speed of wavefront measurement was limited by the low frame rates of conventional cameras. In addition, these cameras used most of their bits to represent an informationless background when the signal-to-background ratio was low, resulting in extremely low efficiencies in the use of bits. Here, using a lock-in camera, we increase the bit efficiency and reduce the data transfer load by digitizing only the signal after rejecting the background. With this camera, we obtained the wavefront of ultrasonically tagged light after a single frame of measurement taken within 0.3 ms, and focused light in between two diffusers. The phase sensitivity has reached 0.51 rad even when the SBR is 6×10^{-4}.   © 2016 Optical Society of America

Focusing light inside biological tissue is critical in many applications, such as high-resolution fluorescence imaging, photodynamic therapy, non invasive optogenetics, laser surgery, and optical tweezers. However, the scattering of light in tissue prohibits focusing light beyond the optical diffusion limit–around 1 mm deep inside the tissue [1–3]. To break this limit, time-reversed ultrasonically encoded (TRUE) optical focusing was developed [4–6]. Unlike iterative wavefront shaping methods [7,8], this technique finds the optimum wavefront without iteration. Moreover, it controls more than 10^5 degrees of freedom, which are much larger than that controlled in adaptive optics, thus enabling focusing deeper inside scattering media [4–6]. Analog TRUE focusing systems based on photorefractive

crystals can tolerate fast speckle decorrelation as short as 5.6 ms [9]. However, the energy gain is low—the phase-conjugated light is much weaker than the light originally coming out of the ultrasonic guide star. In comparison, digital TRUE focusing systems [5,6,10–13] have a much higher energy gain ($\sim 10^5$), and by synthesizing the wavefront, they can even focus light to the single optical speckle scale [14].

In previous digital TRUE focusing systems, a conventional camera records four interference patterns that are transferred to a computer to calculate the wavefront of ultrasonically tagged light (T) (a method known as phase-shifting holography [15]). The conventional camera is highly inefficient in its use of bits and limits the speed of the wavefront measurement, which can be understood as follows. To measure the wavefront of T using phase-shifting holography, a camera records the light patterns formed by a planar reference beam (R), T, and untagged light (U) at a frame rate of $4f_b$ [Figs. 1(a) and 1(b)], when T and R beat at a frequency of f_b. The averaged light intensity recorded by each camera pixel can be expressed as $I(\vec{r}, t) = I_R + I_T(\vec{r}) + I_U(\vec{r}) + 2\sqrt{I_R I_T(\vec{r})} \cos[2\pi f_b t + (\varphi_T(\vec{r}) - \varphi_R)]$. Here, I_R, I_T, and I_U are the intensities of R, T, and U, respectively; φ_T and φ_R are the phases of T and R. $I(\vec{r}, t)$ can be decomposed as $I(\vec{r}, t) = I_{DC}(\vec{r}) + S_{AC}(\vec{r}, t)$ [Fig. 1(c)], where $I_{DC}(\vec{r}) = I_R + I_T(\vec{r}) + I_U(\vec{r})$ and $S_{AC}(\vec{r}, t) = 2\sqrt{I_R I_T(\vec{r})} \cos[2\pi f_b t + (\varphi_T(\vec{r}) - \varphi_R)]$. $S_{AC}(\vec{r}, t)$ is related to the phase map $\varphi_T(\vec{r})$ we want to measure, and it oscillates at f_b, while $I_{DC}(\vec{r})$ is a static background that does not contain useful phase information. Therefore, the signal-to-background ratio (SBR) can be expressed as $SBR = amp(S_{AC})/I_{DC} = 2\sqrt{I_R I_T}/(I_R + I_T + I_U)$, where $amp(\cdot)$ denotes taking the amplitude. When the targeted focusing location is deep and a high-frequency ultrasonic transducer is used for a small focal volume, due to the large amount of untagged light compared with tagged light, the SBR can be extremely low. For example, in a simulation of focusing 10 mm deep inside a chicken breast, using a 50 MHz transducer and 800 nm laser illumination, the SBR was found to be $\sim 10^{-4}$ [16]. When the SBR is lower than
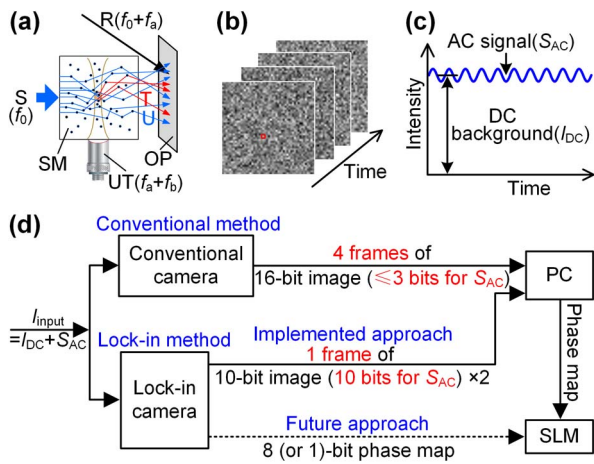
Fig. 1. (a) Illustration of different components of light that are detected by a camera. f_0, laser frequency; f_a, central frequency of ultrasonic transducer; f_b, beat frequency between R and T; OP, the object plane imaged by a camera to measure the wavefront of T; R, reference beam; S, sample beam; SM, scattering medium; T, ultrasonically tagged light, which has a frequency of $f_0 + f_a + f_b$; UT, ultrasonic transducer; U, untagged light, which is not modulated by ultrasound and whose frequency is f_0. (b) The light intensity patterns on plane OP at various times. (c) Light intensity as a function of time for the pixel denoted by the red square in (b). A small AC signal (with a frequency of f_b) sits on a very large DC background. (d) A comparison between using a conventional camera and using a lock-in camera to achieve TRUE focusing. The wavefront of T is measured by phase-shifting holography or our lock-in method, then, the conjugate phase map is displayed on a phase-only spatial light modulator (SLM) to phase conjugate T back to the ultrasonic focus. PC, personal computer.

10^{-4}, even with a 16 bit analog-to-digital converter (ADC), no more than 3 bits of a pixel value can be used to represent the signal (S_{AC}), while most of the bits are wasted in representing the informationless background (I_{DC}). Besides this low efficiency in the use of bits, all of the 16 bit data, including both the signal and the background, are transferred to a computer, which increases the data transfer load [Fig. 1(d)]. Even worse, phase-shifting holography needs to record and transfer at least four frames of images to calculate the phase map on a computer, so the speed of wavefront determination is severely limited by the low frame rates of conventional cameras and the heavy load during data transfer. When averaging is needed, even more frames need to be recorded and transferred, so it takes seconds to acquire a phase map (with 1920×1080 pixels) before time-reversed focusing can be performed in previous works [5,6,11,12]. To apply this technique *in vivo*, systems with higher speeds are strongly desired to accommodate the fast speckle decorrelation (on a time scale from 0.1 ms to 1 ms) primarily due to blood flow [9].

In this work, we developed a wavefront measurement method based on a lock-in camera [17,18] (heliCam C3, Heliotis; 300×300 pixels), in which each pixel performs analog lock-in detection and outputs only the information of the AC signal (S_{AC}) at up to 3800 frames per second to an on-chip memory. Specifically, the lock-in circuitry generates the in-phase ($S_I(r) \propto 2\sqrt{I_R I_T(\vec{r})} \sin[(\varphi_T(\vec{r}) - \varphi_R + \pi/4)]$) and the

quadrature ($S_Q(r) \propto 2\sqrt{I_R I_T(\vec{r})} \cos[(\varphi_T(\vec{r}) - \varphi_R + \pi/4)]$) components of the AC signal oscillated at the frequency of f_b, which are then digitized by a 10 bit ADC. Since only the information of the AC signal, not that of the DC background, is digitized, the lock-in camera tremendously increases the bit efficiency by using all of the bits to represent the signal, and it enables the use of inexpensive low-resolution ADCs. Moreover, compared with the previous method that needs to record and transfer four frames, our approach can obtain the desired phase map after only a single frame of measurement taken within 0.3 ms. It also reduces the data transfer load by transferring only one frame of the information of the signal, instead of four frames of raw images composed of both the signal and the background.

The lock-in camera has two related output modes [Fig. 1(d)]. In Mode A, S_I and S_Q for each pixel are transferred to a computer via a USB 2.0 interface. In Mode B, the desired phase map, $\varphi_T(\vec{r}) - \varphi_R + \pi/4$, calculated by an on-chip field-programmable gate array (FPGA) is directly transferred to a computer. Compared with Mode A, Mode B minimizes the data transfer load and removes the need for a computer to calculate the phase map; therefore, it is ideal for high-speed TRUE focusing systems. However, since our camera is designed for other applications, Mode B outputs some other data irrelevant for our applications, transferring more data than Mode A. Because the speed is currently limited by the data transfer rate of USB 2.0, we chose to use Mode A. In all our experiments, R was shined normally to the surface of the camera, so φ_R was approximately a constant. f_b was experimentally optimized to 70 kHz for maximum sensitivity. The lock-in camera locked-in 20 cycles of the beat signal at frequency f_b, and output one frame of data comprising S_I and S_Q for each pixel. The phase map was calculated on a computer by $\varphi_T(\vec{r}) = \arg(S_I/S_Q)$ based on the data from a single frame measured within 0.3 ms. Here, $\arg(\cdot)$ denotes taking the argument, and the uniform phase offset $-\varphi_R + \pi/4$ has been dropped.

We tested the lock-in camera by measuring two standard wavefronts. A continuous-wave laser at 532 nm (Verdi V5, Coherent) was used in all our experiments. For a plane wave with an incidence angle of –5' relative to the z axis [Fig. 2(a)], the measured phase map is shown in Fig. 2(b), which manifests a plane wave at an oblique incidence. For a spherical wave generated by lens focusing [Fig. 2(c)], the measured phase map shows concentric rings, as expected [Fig. 2(d)]. The ghost rings surrounding the central rings are due to the spatial aliasing effect, since the widths of the central rings become narrower than the pixel size of the lock-in camera beyond a certain radius.

To characterize the phase sensitivity of the lock-in camera as a function of the SBR, we used the camera to measure the spatial light modulator (SLM) encoded wavefront of a sample beam (S). The ratio between the intensity of S (I_S) and R (I_R) was controlled by neutral density filters with different transmittances [Fig. 3(a)]; SBR $= 2\sqrt{I_S I_R}/(I_S + I_R)$. The left half of the SLM displayed $\pi/4$, while the right half displayed $-\pi/4$. To remove the background in the measured phase map caused by the SLM's curvature and the wavefront mismatch between R and S, the phase map measured when the SLM displayed all zeros was subtracted from the measured phase map. The phase maps measured when the SBR ranged from 6×10^{-3} to 6×10^{-5} are shown in Fig. 3(b). When the SBR was between one and 2×10^{-2}, the measured phase maps resemble the phase
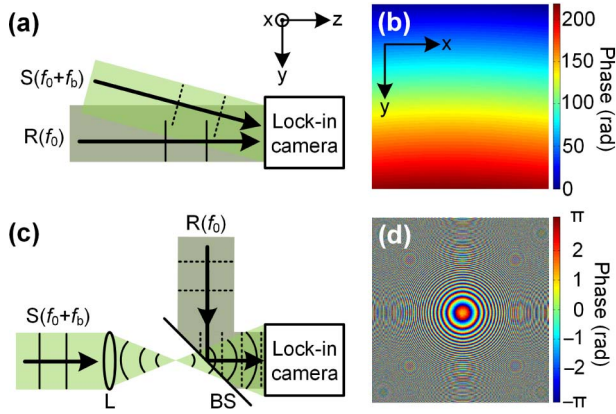
Fig. 2. (a) Schematic of the set-up to measure the wavefront of an oblique incident plane wave, and (b) the measured phase map. (c) Schematic of the set-up to measure the wavefront of a spherical wave, and (d) the measured phase map. BS, beamsplitter; f_0, laser frequency; f_b, beat frequency between R and S; R, reference beam; S, sample beam.

map measured when the SBR $= 6 \times 10^{-3}$, so they are not shown. The phase sensitivity (defined as the standard deviation of the left half of the measured phase map) and the difference of the mean phase between the left and right halves of the phase map are shown as a function of the SBR in Fig. 3(c). With decreasing SBR, the phase sensitivity degrades due to the decreasing signal-to-noise ratio (SNR), and the mean phase difference deviates more from the expected value of $\pi/2$ for
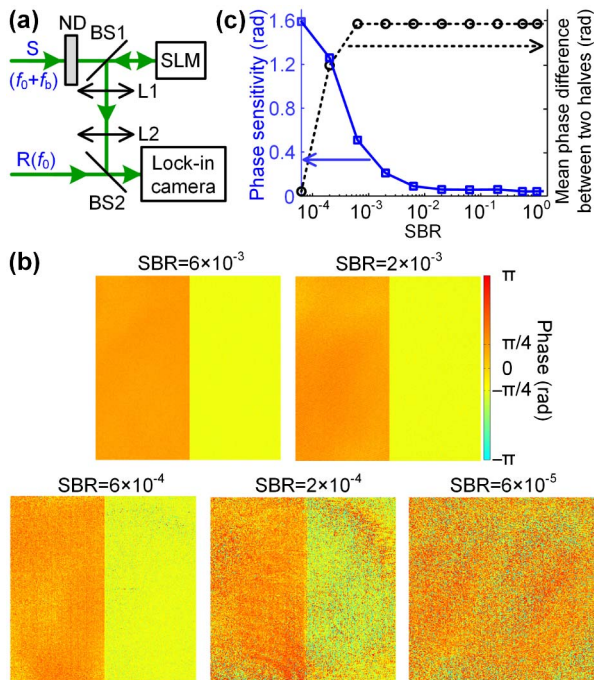

Fig. 3. (a) Schematic of the set-up to characterize the phase sensitivity of the lock-in camera as a function of the signal-to-background ratio (SBR). ND, neutral density filters; SLM, spatial light modulator. (b) The phase maps measured at different SBRs. (c) The phase sensitivity and the difference of the mean phase between the left and right halves of the phase map as a function of SBR.

the same reason. The phase sensitivity has reached 0.51 rad even when the SBR is 6×10^{-4}. To obtain the data in Fig. 3(c), as the SBR decreased from one to 6×10^{-5}, the light power at the image sensor was set to 1, 1, 4, 8, 17, 44, 120, 120, 120, and 120 mW. Higher power was used to increase the SNR when the SBR was low, but the power did not exceed 120 mW, to avoid camera saturation.

Based on the lock-in camera, we developed a TRUE focusing system [Fig. 4(a)] to focus light inside a scattering medium composed of two ground glass diffusers (D1 and D2). Our focusing procedure included two steps. In the first step, the wavefront $\varphi_T(\vec{r})$ was measured using the lock-in camera with a Mach–Zehnder interferometer. After passing through an acousto-optic modulator, the frequency of R became $f_0 + f_a$, where $f_a = 50$ MHz, and f_0 was the laser frequency. In the sample arm, after passing through D1, the frequency of a portion of the diffuse light traversing the ultrasonic focus was shifted to $f_0 + (f_a + f_b)$, due to the acousto-optic effect, where $f_a + f_b = 50$ MHz $+70$ kHz was the frequency of the ultrasound generated from an ultrasonic transducer with a 0.4 numerical aperture. The driving voltage to the transducer was 20 V, and the ultrasound was present only during the exposure time (0.286 ms) of the lock-in camera. S then passed through D2, collected by lens L5, and combined with R by a 50/50 beamsplitter (BS), BS2. Then, the combined beams were reflected from an SLM (Pluto NIR-II, Holoeye) and were further directed to
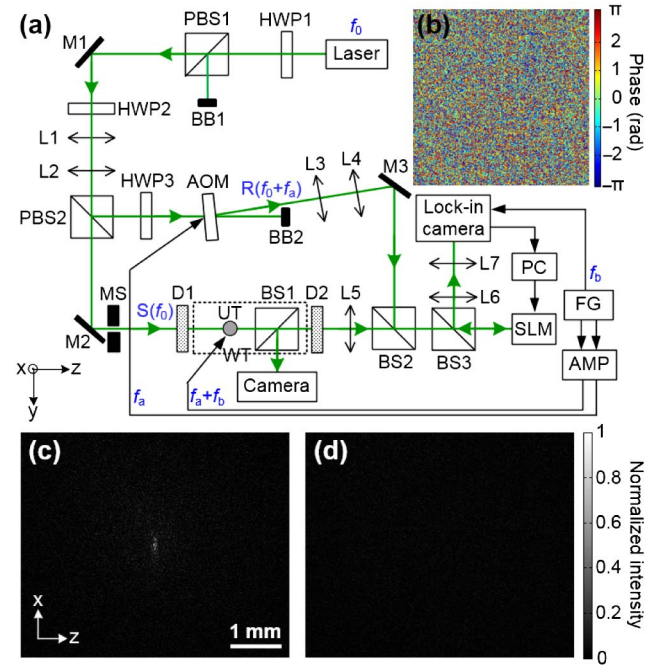

Fig. 4. Lock-in camera based TRUE optical focusing. (a) Schematic of the set-up. AMP, power amplifier; AOM, acousto-optic modulator; BB, beam block; BS, beamsplitter; D, diffuser; FG, function generator; HWP, half-wave plate; L, lens; M, mirror; PC, personal computer; SLM, spatial light modulator; PBS, polarizing beamsplitter; UT, ultrasonic transducer; WT, water tank. (b) The conjugate wavefront of T, which was displayed on the SLM. (c) The observed TRUE focus when the SLM displayed the phase map in (b). (d) When the correct phase map was shifted leftward by 1 super pixel (3 SLM pixels), the TRUE focus disappeared.

the lock-in camera by a 50/50 BS, BS3. The lock-in camera imaged the surface of the SLM by a $4f$ system with a magnification of 5/3, and each camera pixel imaged a super pixel (3×3 pixels) on the SLM. The lock-in camera locked in the beat frequency $f_b = 70$ kHz and, thus, measured the phase map of T. In the second step, we achieved digital TRUE focusing by phase conjugating T. In this step, S was blocked, and we displayed $-\varphi_T(\vec{r})$ on the SLM [Fig. 4(b)]. Upon reflection from the SLM, R acquired a wavefront $-\varphi_T(\vec{r})$, thus becoming phase conjugated to T. After passing through D2, the phase-conjugated light converged to the original ultrasonic focal position (No ultrasound was applied in this step). To visualize the TRUE focus, we placed a 10/90 BS, BS1, in between D2 and the ultrasonic focal position to produce a copy of the optical focus that was measured by a camera.

The observed TRUE focus is shown in Fig. 4(c), and it disappeared when the correct phase map on the SLM was shifted leftward by 1 super pixel ($=3$ pixels) [Fig. 4(d)], as expected. In Fig. 4(c), the full width at half-maximum (FWHM) focal spot size along the y direction was 58 μm, which is close to the 47 μm measured acoustic focal spot size along the transverse direction. The FWHM focal spot size along the x direction (the acoustic axis direction) was 262 μm, which is smaller than the measured depth of focus of the acoustic focal zone ($=336$ μm). The peak-to-background ratio (PBR), defined as the ratio between the average intensities within and outside the TRUE focus, was 12, which is about 30 times lower than its theoretical value. The discrepancy between the measured and the theoretical PBR is probably due to imperfect alignment.

In our TRUE focusing experiment, the SBR was measured to be 6×10^{-3}, which was comparable with the SBR achieved in a previous TRUE focusing experiment using a scientific CMOS camera [11]. Currently, the sample arm was very lossy (only ~1/1000 of the light power incident on the sample arrived at the camera), which limited the available light power on the lock-in camera. To accommodate even lower SBRs for deeper penetration or more scattering samples by increasing the SNR, a stronger laser and higher collection efficiency for the diffuse light are needed.

Currently, even though the wavefront is measured within 0.3 ms, it takes ~12 ms to transfer the data from the lock-in camera to a computer, limited by the speed of the USB 2.0 interface (~250 Mb/s). If a camera link interface is used (data transfer rate ~7024 Mb/s), the data transfer time can be reduced to 0.4 ms. Moreover, rather than outputting S_I and S_Q, the camera can also directly output a 16 bit phase map calculated by the on-chip FPGA, which reduces the data transfer load and removes the need to calculate the phase map on a computer. Since digital optical phase conjugation has a high tolerance for phase error [19], 8 bits rather than 16 bits are sufficient to represent a phase value, so we can further decrease the data transfer time by half to 0.1 ms by using an 8 bit ADC. Currently, it takes ~30 ms to display a phase map on the SLM, which is the bottleneck of speed in our whole TRUE focusing procedure. Because SLMs with binary modulation, such as digital micromirror devices [20–22], are much faster than our gray-scale SLM, we plan to modify the FPGA program on the camera to output a binary phase map (1 bit per pixel) directly to a binary modulation SLM [Fig. 1(d)]. In this way, we can further decrease the data transfer load by eight times.

In conclusion, based on a lock-in camera, we developed a method to quickly measure the wavefront of light in a low SBR condition, and applied it to TRUE optical focusing inside scattering media. Since the lock-in camera digitizes only the signal after rejecting the background, our method is highly efficient in the use of bits, and has the potential to achieve a very large data reduction at an early stage to minimize the data transfer load. Combined with a binary modulation SLM, our approach can potentially complete the TRUE focusing procedure within 1 ms, which will enable many *in vivo* applications that require light focusing deep inside tissue. Compared with other wavefront sensors, such as the Shack-Hartmann sensor, our sensor has much greater resolution (300×300 pixels versus 11×11 pixels [23]). Moreover, our high-speed wavefront measurement method is readily applicable to other time-reversal based focusing techniques [24,25]. Since the lock-in camera can also measure the amplitude of an AC signal on each pixel in parallel in a low SBR condition, it is an excellent choice for ultrasound-modulated optical tomography (also called acousto-optic imaging).

REFERENCES

1. V. Ntziachristos, Nat. Methods **7**, 603 (2010).
2. L. V. Wang and H. Wu, *Biomedical Optics: Principles and Imaging* (Wiley, 2007).
3. Y. Liu, C. Zhang, and L. V. Wang, J. Biomed. Opt. **17**, 126014 (2012).
4. X. Xu, H. Liu, and L. V. Wang, Nat. Photonics **5**, 154 (2011).
5. Y. M. Wang, B. Judkewitz, C. A. DiMarzio, and C. Yang, Nat. Commun. **3**, 928 (2012).
6. K. Si, R. Fiolka, and M. Cui, Nat. Photonics **6**, 657 (2012).
7. I. M. Vellekoop and A. P. Mosk, Opt. Lett. **32**, 2309 (2007).
8. M. Cui, Opt. Express **19**, 2989 (2011).
9. Y. Liu, P. Lai, C. Ma, X. Xu, A. A. Grabar, and L. V. Wang, Nat. Commun. **6**, 5904 (2015).
10. K. Si, R. Fiolka, and M. Cui, Sci. Rep. **2**, 748 (2012).
11. Y. Suzuki, J. W. Tay, Q. Yang, and L. V. Wang, Opt. Lett. **39**, 3441 (2014).
12. Y. Suzuki and L. V. Wang, Appl. Phys. Lett. **105**, 191108 (2014).
13. H. Ruan, M. Jang, B. Judkewitz, and C. Yang, Sci. Rep. **4**, 7156 (2014).
14. B. Judkewitz, Y. M. Wang, R. Horstmeyer, A. Mathy, and C. Yang, Nat. Photonics **7**, 300 (2013).
15. I. Yamaguchi and T. Zhang, Opt. Lett. **22**, 1268 (1997).
16. M. Jang, H. Ruan, B. Judkewitz, and C. Yang, Opt. Express **22**, 5787 (2014).
17. S. Bourquin, P. Seitz, and R. P. Salathé, Opt Lett **26**, 512 (2001).
18. R. Patel, S. Achamfuo-Yeboah, R. Light, and M. Clark, Opt. Express **19**, 24546 (2011).
19. M. Cui and C. Yang, Opt Express **18**, 3444 (2010).
20. D. Wang, E. H. Zhou, J. Brake, H. Ruan, M. Jang, and C. Yang, Optica **2**, 728 (2015).
21. C. Ma, F. Zhou, Y. Liu, and L. V. Wang, Optica **2**, 869 (2015).
22. D. B. Conkey, A. M. Caravaca-Aguirre, and R. Piestun, Opt. Express **20**, 1733 (2012).
23. X. Tao, Z. Dean, C. Chien, O. Azucena, D. Bodington, and J. Kubby, Opt. Express **21**, 31282 (2013).
24. C. Ma, X. Xu, Y. Liu, and L. V. Wang, Nat. Photonics **8**, 931 (2014).
25. E. H. Zhou, H. Ruan, C. Yang, and B. Judkewitz, Optica **1**, 227 (2014).